

# Kinematics of massive stars in the Small Magellanic Cloud

Christopher J. Evans<sup>1\*</sup> & Ian D. Howarth<sup>2</sup>

<sup>1</sup>*UK Astronomy Technology Centre, Royal Observatory Edinburgh, Blackford Hill, Edinburgh, EH9 3HJ, UK*

<sup>2</sup>*Department of Physics & Astronomy, University College London, Gower Street, London WC1E 6BT, UK*

Accepted by MNRAS

## ABSTRACT

We present radial velocities for 2045 stars in the Small Magellanic Cloud (SMC), obtained from the 2dF survey by Evans et al. (2004). The great majority of these stars are of OBA type, tracing the dynamics of the young stellar population. Dividing the sample into *ad hoc* ‘bar’ and ‘wing’ samples (north and south, respectively, of the line:  $\delta = -77^\circ 50' + [4\alpha]'$ , where  $\alpha$  is in minutes of time) we find that the velocities in the SMC bar show a gradient of  $26.3 \pm 1.6 \text{ km s}^{-1} \text{ deg}^{-1}$  at a position angle of  $126 \pm 4^\circ$ . The derived gradient in the bar is robust to the adopted line of demarcation between the two samples. The largest redshifts are found in the SMC wing, in which the velocity distribution appears distinct from that in the bar, most likely a consequence of the interaction between the Magellanic Clouds that is predicted to have occurred 0.2 Gyr ago. The mean velocity for all stars in the sample is  $+172.0 \pm 0.2 \text{ km s}^{-1}$  (redshifted by  $\sim 20 \text{ km s}^{-1}$  when compared to published results for older populations), with a velocity dispersion of  $30 \text{ km s}^{-1}$ .

**Key words:** galaxies: kinematics and dynamics – galaxies: Magellanic Clouds – stars: early-type – stars: fundamental parameters

## 1 INTRODUCTION

By studying the kinematic and chemical characteristics of the Milky Way and nearby galaxies, past interactions and the history of mass assembly can be explored. The Magellanic Clouds are of particular interest in this context as their dynamical evolution and star-formation histories appear to be closely entwined (e.g., Yoshizawa & Noguchi 2003). For instance, the Magellanic Stream has generally been thought to arise from tidal disruption by the Milky Way (Gardiner & Noguchi 1996; Putman et al. 1998; Connors et al. 2006), although new proper motion results (Kallivayalil et al. 2006) suggest that the Clouds may be on their first passage about the Milky Way, calling into question the origins of the Stream (Besla et al. 2007).

From observations of the neutral-hydrogen gas, Mathewson & Ford (1984) advanced the concept that the SMC is comprised of two components, with a ‘Mini-Magellanic Cloud’ being effectively torn off by a past interaction with the LMC, leaving the remnant of the SMC. These components had been identified previously by McGee & Newton (1981), who also noted additional features at larger and smaller velocities. Observations of the H I gas at better spatial resolution (Staveley-Smith et al. 1997) have revealed a much more complex structure, comprised of hun-

dreds of expanding shells, presumably driven by stellar-wind outflows and supernovae, which led the authors to describe the SMC as ‘distinctly frothy and filamentary’. Subsequent observations of three large supershells were reported by Stanimirović et al. (1999), with the most dominant of these, 304A, potentially accounting for the twin components seen previously in the main body of the SMC.

To date, the most comprehensive survey of stellar kinematics in the SMC is the study of 2046 red giants by Harris & Zaritsky (2006), who concluded that this old population is supported by its velocity dispersion (rather than rotation). Previous, more limited, studies have focussed on luminous supergiants (Ardeberg & Maurice 1977, 1979; Maurice et al. 1987), Cepheids (Mathewson et al. 1988), and on the older stellar populations, e.g., carbon stars (Hatzidimitriou et al. 1997; Kunkel et al. 2000) and red-clump stars (Hatzidimitriou et al. 1993).

The proximity and significantly sub-solar metallicity of the Clouds have also made them popular targets for spectroscopic studies of stellar evolution. This was the primary motivation for our own spectroscopic survey of the young, blue population of the Small Magellanic Cloud (Evans et al. 2004, hereinafter Paper I), which resulted in spectral classifications for 4161 stars, dominated by early (OBA) types. Here we present radial velocities for 2045 objects from that sample, covering a relatively wide spatial area (including the ‘wing’ region) and providing kinematic information for

\* email: cje@roe.ac.uk, idh@star.ucl.ac.uk

a component of the SMC population which has previously gone largely unexplored.

## 2 STELLAR RADIAL VELOCITIES

Our spectroscopic survey used the 2-degree-field instrument at the Anglo-Australian Telescope (2dF at the AAT). 2dF was a multi-fibre instrument which allowed up to 400 intermediate-dispersion spectra to be recorded simultaneously, using two spectrographs (Lewis et al. 2002). The main observing programme consisted of 18 fields observed in two runs: 1998 September and 1999 September (fields 1–12 and 13–18, respectively). The survey area is shown in Fig. 1.

Our spectra all cover at least the wavelength range  $\sim 3900\text{--}4800\text{\AA}$  (with about half including  $H\beta$ ) at a resolving power of  $R \simeq 1600$  ( $\Delta v \simeq 190\text{ km s}^{-1}$ ), with signal-to-noise ratios in the range 20–150 (see Paper I for details). While the data were not optimized for very precise studies of velocities for individual stars, the moderately large sample, and extensive spatial coverage, encouraged us to investigate global trends in the overall kinematics.

The 4161 observed targets cover a moderately wide range in spectral type (with classifications from mid O-type to, in a few cases, late G-type), and hence also in temperature and in spectral morphology. Although we compiled radial-velocity measurements using semi-automated procedures, we found that, as a consequence of this range and of variations in data quality, ‘manual’ measurements gave better results. Compelled to use strong lines because of signal-to-noise constraints, we measured heliocentric velocities for  $H\beta$ ,  $H\gamma$ ,  $H\delta$ ,  $H8$ , and  $H9$  ( $H\epsilon$  was excluded due to blending with  $\text{Ca II H}$ ). It is these results that we report here.

Many of the spectra show emission in the lower members of the Balmer series, precluding reliable measurement of the line centres. In the majority of cases this emission is probably nebular in origin, but in some it will be intrinsic to the star. Affected spectra were excluded from the outset, leaving 3369 stars with three or more ‘good’ lines.

### 2.1 External sources of error

Our data are free from one common source of radial-velocity error, namely mis-centring of the target in the slit, because of ‘scrambling’ of the signal by the fibre runs. However, the two 2dF spectrographs were mounted on the top-end ring of the AAT, bringing other external factors, such as flexure, into the radial-velocity uncertainties. Such factors are well known to 2dF users (though not well documented), with a signature of obvious problems being offsets in the velocity zero-points between the two spectrographs (e.g., the unpublished technical report by Stanford & Cannon 2002<sup>1</sup>).

Velocities from the two spectrographs appear well matched in our data throughout 1999 (as judged from comparison of the median velocities from the two sets of different targets observed simultaneously at a given telescope pointing). However, the 1998 observations show poorer agreement, with offsets of up to  $\sim 100\text{ km s}^{-1}$  between spectrographs (Fig. 2). We rejected all fields where median velocities

from the two spectrographs differ by more than  $30\text{ km s}^{-1}$ , leaving results from 11 fields (3, 5, 6, 8, 9, 13–18) with a mean offset (Spec1–Spec2) of  $+3.1 \pm 14.1$  (s.d.)  $\text{km s}^{-1}$ . (A cut at  $20\text{ km s}^{-1}$  further excludes fields 8 and 9, but has no material effect on any results.)

We also used measurements of 66 stars from ancillary spectra obtained in 2002; although these were taken in only one spectrograph, the observations (described by Harries et al. 2003) were designed for radial-velocity measurements, and repeat observations show a scatter consistent with internal errors alone. This gives a final sample of 2045 stars, for which results are tabulated in Appendix A.

### 2.2 Internal uncertainties

Data given in the Appendix include the standard error on the mean of the measurements for each star (i.e.  $\sigma/\sqrt{n}$ , where  $n$  is the number of measured lines). The mean standard error from 2045 stars is  $11.1\text{ km s}^{-1}$ , which provides an estimate of the purely internal uncertainty of our velocities. Only  $\sim 3\%$  of stars have standard errors greater than  $25\text{ km s}^{-1}$ , and these can generally be attributed to low signal-to-noise spectra, or to unrecognized nebular contamination.

Velocities are available from two separate 2dF observations for only 24 targets from the 2045-star sample; results are shown in Fig. 3 (which includes, for completeness, results for an additional 14 stars with observations from rejected fields). The pairs of observations are distributed among 14 field/spectrograph combinations, so that it is impractical to try to establish separately any systematic offsets from these data. Instead, we simply compute the mean absolute difference between observations of each target:  $12.4 \pm 2.1$  (s.e.)  $\text{km s}^{-1}$ . It can be shown that the implied  $1\text{-}\sigma$  uncertainty on a single observation is a factor 0.886 smaller; i.e.,  $11.0 \pm 1.9\text{ km s}^{-1}$ . This ‘internal error’ estimate incorporates any contributions from plate-to-plate zero-point shifts and astrophysical variability in radial velocity, in addition to stochastic uncertainties in the measurements; the excellent agreement with the value given in the preceding paragraph therefore implies that stochastic uncertainties dominate.

### 2.3 External checks

Of independent results at our disposal, the high-resolution ( $R \sim 20,000$ ,  $\Delta v \simeq 15\text{ km s}^{-1}$ ) VLT-FLAMES survey of massive stars in two SMC fields by Evans et al. (2006) offers both the largest overlap with the 2dF data, and the highest-quality data. A comparison between 2dF and FLAMES velocities for 28 apparently single stars is shown in Fig. 4. There is excellent overall agreement, with a mean offset of  $-7\text{ km s}^{-1}$  (FLAMES–2dF). The standard errors of the FLAMES velocities are small (typically  $2\text{--}3\text{ km s}^{-1}$ ); if the errors add quadratically, and if none of the stars has intrinsic radial-velocity variations, the dispersion in differential velocities ( $14\text{ km s}^{-1}$ ) provides an upper limit to the statistical uncertainty of the 2dF results of  $13.5\text{ km s}^{-1}$ .

We have provisional velocities for a further 13 stars from a follow-up FLAMES study of the SMC cluster NGC 346, at lower resolution ( $R \sim 7,000$ ,  $\Delta v \simeq 42\text{ km s}^{-1}$ ; Evans et al., in preparation). Results for these stars are in reasonable agreement with the 2dF values (Fig. 4), excepting

<sup>1</sup> <http://www.aao.gov.au/AAO/2df/technotes/fibvel.ps.gz>

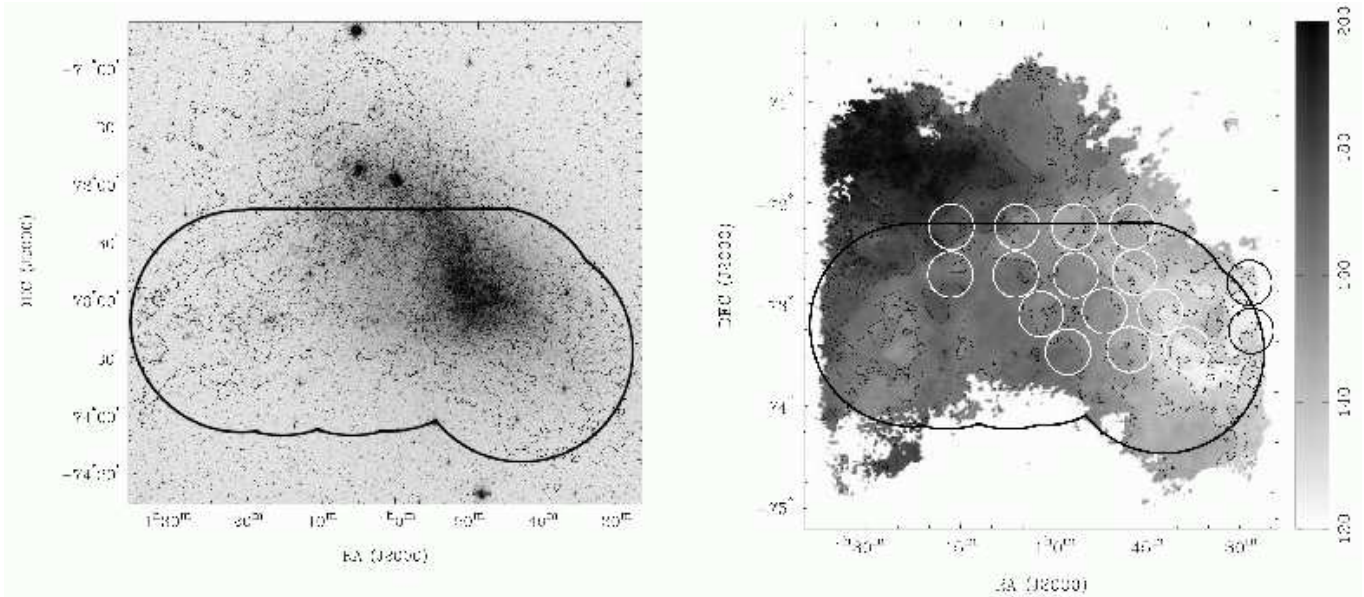


**Figure 1.** The approximate boundaries of the 2dF SMC survey, superimposed on a  $V$ -band image by M. Bessel (left; contours show H I column densities), and on an H I velocity map (right; small circles show fields observed by Harris & Zaritsky 2006). The dense optical region constitutes the SMC bar, with the Wing being the lower-density eastern region. Adapted, with permission, from Stanimirović et al. (2004).

four O9.5–B1 stars which have FLAMES velocities that are rather smaller than 2dF values (by  $\sim 40$ – $70$  km s $^{-1}$ ); these stars lead to a relatively large dispersion in the velocity differences. It is not implausible that these could all be single-lined binaries (even though there is only a 1 in 8 probability of all four stars having velocity offsets in the same direction).

Differential velocities are also shown in Fig. 4 for 18 A-type supergiants/bright giants observed with the AAT’s RGO spectrograph at  $R \sim 2,700$  (Evans & Howarth 2003); in these relatively cooler, less massive stars, effects such as nebular contamination and binarity would not be expected to be as important as in the OB samples. The 2dF measurements show a  $\sim 20$  km s $^{-1}$  offset (in the same sense as found for the FLAMES comparison), which is only  $\sim 10\%$  of the combined resolution elements of the two datasets. If we suppose that the dispersion in velocity differences between the 2dF and RGO spectra arises from these datasets in inverse proportion to their resolutions, the implied statistical uncertainty on 2dF measurements is  $\sim 15$  km s $^{-1}$ .

We also found three other apparently good-quality velocities in the recent literature for seemingly single stars in common with the 2dF sample. These are AzV 170 (Walborn et al. 2000, 2dFS#1086), AzV 215 (Trundle et al. 2004,<sup>2</sup> 2dFS#1352) and AzV 235 (Evans et al. 2004, 2dFS#1416, where ‘2dFS’ numbers are from the catalogue of Paper I). Results are included in Fig. 4.

The results of all these velocity comparisons are summarized in Table 1. All the indications are that the  $1\text{-}\sigma$  statistical uncertainties in our 2dF velocities are  $\sim 13 \pm 2$  km s $^{-1}$ . There is some evidence that the 2dF results may be system-

**Table 1.** Comparison of 2dF radial velocities from repeat exposures, and with those from external sources (discussed in Section 2.3). Tabulated velocity differences are in the sense ‘source’ minus 2dF. All targets used in the comparisons are OB stars, except for the RGO-spectrograph sample which is comprised of A-type stars.

Source	$R$	$N$	$\overline{\Delta(v_r)}$	$\sigma$ [km s $^{-1}$ ]	Median
2dF	1600	24		13	
FLAMES (HR)	20 000	28	−7	14	−9
FLAMES (LR)	7000	13	−25	21	−20
RGO	2700	18	−18	17	−20
‘Other’	20 000	3	−19	(4)	−18

atically too positive, by perhaps  $\sim 10$  km s $^{-1}$ , but there is no suggestion that this offset, if real, is a function of time or position. Given the general level of internal consistency demonstrated by Figs. 3 and 4, we are confident that our results are, at the least, internally robust.

### 3 RESULTS

Figure 5 shows the spatial distribution of our sample by velocity bin. By inspection, there is a trend for more positive velocities to the south and east in our sample; in particular, the wing region appears to have systematically more positive velocities than the bar. Arbitrarily dividing the sample stars into ‘bar’ and ‘wing’ according to whether they lie north or south of a line:

$$\delta = -77^\circ 50' + (4\alpha)'$$

<sup>2</sup> Trundle et al. (2004; also Trundle & Lennon 2005) label tabulated velocities as ‘ $v_{\text{lsr}}$ ’, but values are actually heliocentric; Dr. C. Trundle, personal communication.

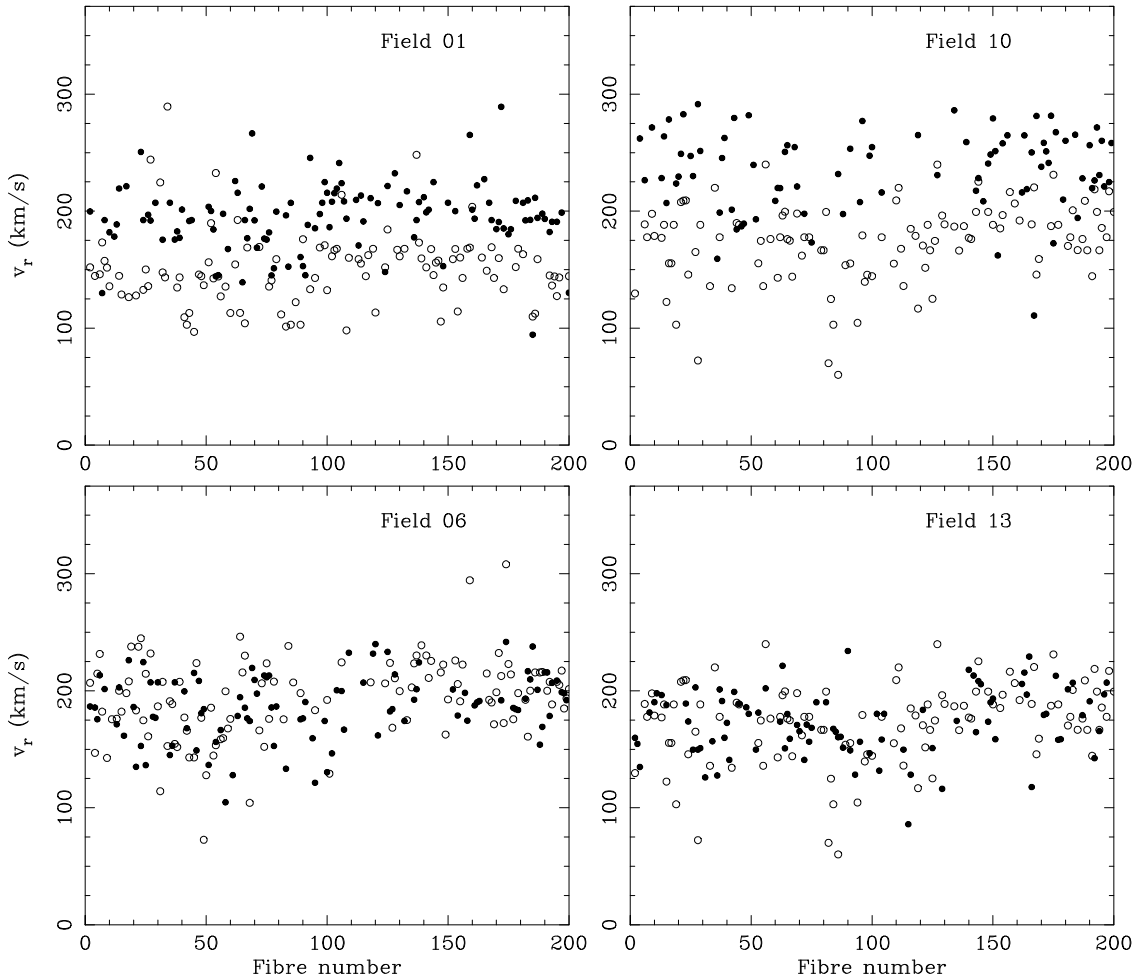


**Figure 2.** Measured radial velocities from survey fields 1, 6, 10 & 13. Solid circles are velocities from spectrograph 1, open circles those from spectrograph 2. Fields 6 and 13 show no important systematic offset; Field 1 and 10 show larger differences (median velocities differ by 47 and 81  $\text{km s}^{-1}$ , respectively), and were excluded from the analysis.

(Fig. 5, where  $\alpha$  is the right ascension in minutes of time), histograms of the 2dF velocities for the two regions are shown in Figure 6. Also shown are the results grouped by spectral type; B-type spectra are grouped as either ‘Early B’ (earlier than B5) or ‘Late B’ (B5, B8 or B9), with the 14 peculiar AF-type stars included with the FG stars.

The most striking feature in Figure 6 is the difference between the velocity distribution of the early B-type stars compared with the later types. The early B-type distribution is near-symmetrical and single-peaked, centred on  $175 \text{ km s}^{-1}$ . This is in strong contrast to the FG stars which appear to have a double-peaked distribution, with maxima at 150 and  $180 \text{ km s}^{-1}$ . This internal comparison reveals different velocity components in the different spectral groups, i.e. with age<sup>3</sup>; the relatively small number of O-type stars

are also peaked at  $\sim 175 \text{ km s}^{-1}$ . The late B-type results appear to have a similar distribution to the FG group, whereas the picture is less clear for the A-type stars.

At first glance the 2dF results appear at odds with the velocities of OBA stars from Maurice et al. (1987), in which a double-peaked structure is seen, with the high-velocity peak much larger. However, their velocities (which include the measurements by Ardeberg & Maurice 1977, 1979) are predominantly from late B- and A-type stars which, when compared to our results in Figure 6, could account for the double-peaked distribution. Moreover, the remainder of the Maurice et al. sample comprises 23 O- and early B-type stars, of which 17 have positive Local Standard of Rest velocities (consistent with our O- and early B-type distributions in Figure 6), giving the larger, high-velocity peak in their results.

One of the more interesting structures reported by Stanimirović et al. (1999, 2004) is the supergiant shell (SGS) 304A. This spans most of the northern region of our observations, with almost 800 of the 2dF stars with radial velocities within the ellipse traced out by the shell (Table 2,

<sup>3</sup> The appearance of the distributions is, of course, a factor of the adopted bin-size. For convenience in Figure 6 we chose  $10 \text{ km s}^{-1}$ . Adopting a bin-size of  $15 \text{ km s}^{-1}$  still reveals a clear difference between the early B- and FG-type results, although the two maxima are less pronounced in the latter distribution.

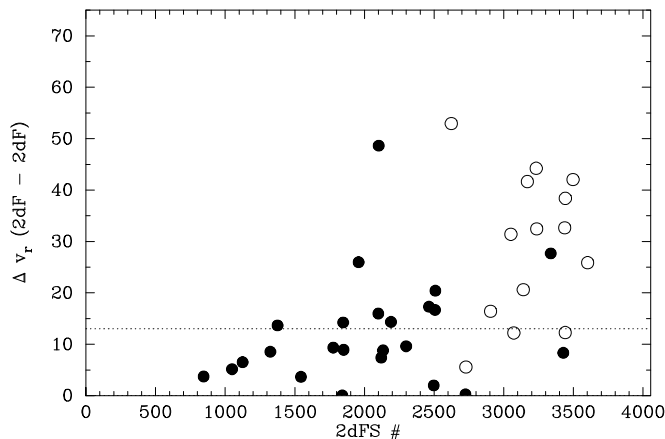


**Figure 3.** Differences in radial velocities from repeat observations with 2dF. Open symbols indicate stars from rejected fields (Section 2.1); the outlying filled symbol (2dFS 2102) may indicate a spectroscopic binary. The horizontal dotted line is drawn at  $13.0 \text{ km s}^{-1}$ , the internal  $1\text{-}\sigma$  error estimated from these data (Section 2.2).

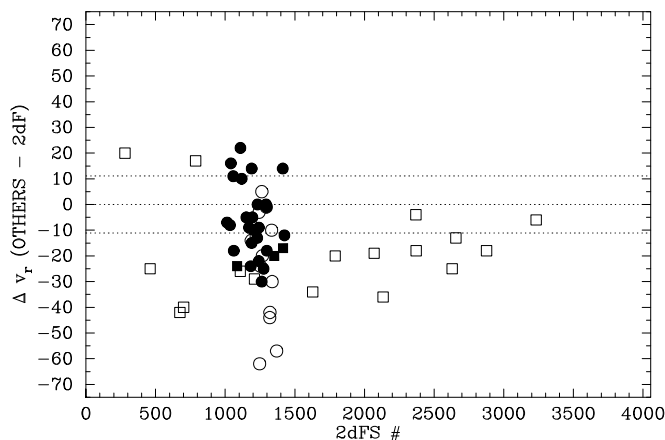


**Figure 4.** Comparison of radial velocities from observations with high-resolution VLT-FLAMES spectra (filled circles, Evans et al. 2006); low-resolution VLT-FLAMES spectra (open circles, Evans et al., in preparation); RGO spectra (open squares, Evans & Howarth 2003); other published high-resolution spectra (filled squares; see Section 2.3 for sources).

Stanimirović et al. 1999). Over half of the stars are O- and early B-type stars, and their velocity distribution is indistinguishable from those in Figure 6. The velocity diagram for SGS 304A shows two distinct components at approximately  $130$  and  $170 \text{ km s}^{-1}$  (Stanimirović et al. 1999), presumably the origin of the offset components reported by McGee & Newton (1981) and Mathewson & Ford (1984). There is significant  $H\alpha$  emission at the edge of SGS 304A (Figure 11, Stanimirović et al. 1999), with N66 (NGC 346, the largest H II region in the SMC) at the northern limit. Indeed, the higher-velocity component is dominant in the R.A.-velocity slice at  $-72^\circ 13' 40''$  (Figure 6, Stanimirović et al. 2004). It appears that the majority of recent star formation in this region, as traced by the 2dF early-type stars, is associated with the higher-velocity component.

The FG stars observed with 2dF must be intrinsically luminous for them if at the distance of the SMC. Detailed luminosity classification of these later-type spectra was beyond the scope of Paper I, however at this point it is of interest to consider their physical luminosities, in order to estimate the range of ages and initial masses probed by the 2dF results. The median magnitude of the observed FG stars, the majority of which are classified as F-type (187 from 229), is  $B = 15.9$ . Adopting  $(B - V)_0 = 0.37$  and a bolometric correction of  $0.11^m$  for a F5 supergiant (e.g. Johnson 1966), together with an SMC reddening of  $E(B - V) = 0.09$  (Massey et al. 1995) and a distance modulus of  $18.91$  (Hilditch et al. 2005), gives  $M_{\text{bol}} \sim -3.5$ . Evolutionary tracks from Charbonnel et al. (1993) then suggest an initial mass of  $\sim 5M_\odot$ , (corresponding to a main-sequence spectral type of  $\sim B2-3$ ) and an age of  $\sim 90-100 \text{ Myr}$ . These are only rough estimates, but they demonstrate that the FG stars are beginning to probe a population significantly older than that traced by the early-type, main-sequence spectra.

### 3.1 Mean velocities

The mean velocities and weighted dispersions, by spectral type, are summarized in Table 2. The OBA-star velocities are significantly more redshifted than results both for our relatively small ‘late-type’ (FG) sample, and for many other older-star samples in the literature, which cluster around  $\sim 150 \text{ km s}^{-1}$  (see the summary in Table 3 of Harris & Zaritsky 2006). The latter difference arises in part because our spatial coverage extends further to the east than many previous studies, which, coupled with the velocity gradient we have found, introduces a positive bias. In particular, Harris & Zaritsky (2006) report  $\bar{v} = 145.6 \pm 0.6 \text{ km s}^{-1}$  for a red-giant population with a mean position about a degree west of that for our sample (Fig. 1), where the mean velocity of the OBA stars is  $\sim 160 \text{ km s}^{-1}$ . While the residual difference is certainly within the combined systematic uncertainties in the two datasets (and is of the size and sign discussed in Section 2.3), it is of interest to note that the mean of the  $\gamma$  velocities determined for 50 eclipsing-binary OB stars by Harries et al. (2003)<sup>4</sup> and Hilditch et al. (2005) is  $+196.2 \pm 24.8 \text{ (s.d.) km s}^{-1}$ . Their sample is, roughly, spatially coincident with Harris & Zaritsky’s, but is a full  $50 \text{ km s}^{-1}$  more redshifted on average.

The difference for the OB stars is in the opposite sense to that which might be expected if the Balmer-line velocities were affected by stellar-wind outflows (which should, if anything, give rise to a blueshifted bias). It remains to be seen how much of this is a consequence of prosaic effects (e.g. unrecognized line blends, or systematic offsets in 2dF spectroscopy), as compared to truly different dynamics for the massive-star population.

#### 3.1.1 Velocities in the K1 region

The K1 region lies to the east of the SMC bar (de Vaucouleurs & Freeman 1972); it is included in our wing sub-

<sup>4</sup> Heliocentric corrections were applied in the wrong sense by Harries et al. (2003; cf. Hilditch et al. 2005); we have corrected their  $\gamma$  velocities by  $+11 \text{ km s}^{-1}$  to allow for this.

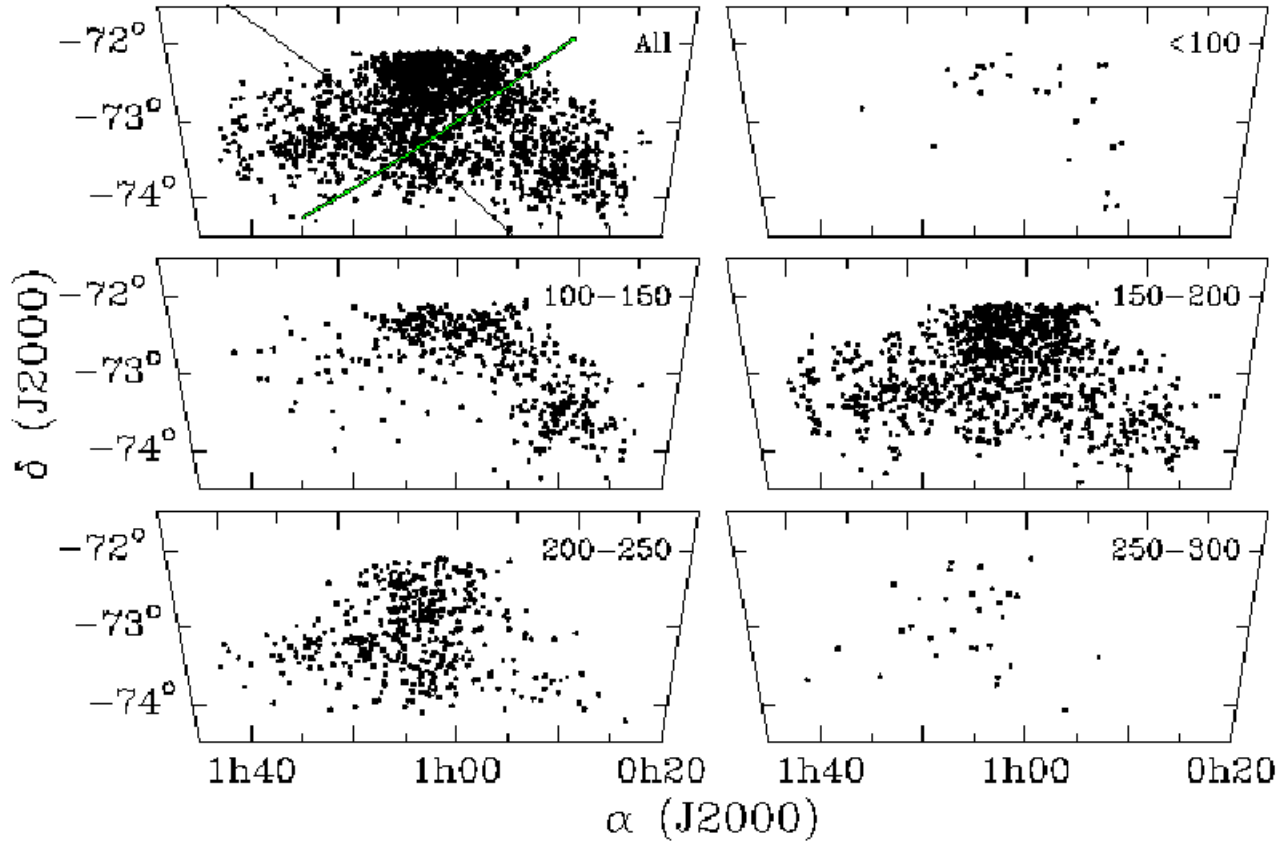


**Figure 5.** Spatial distribution of the 2045 stars with radial velocities from the 2dF survey. The upper-left panel shows the whole sample, with the black line dividing the sample into *ad hoc* subsets of wing and bar stars (Section 3). The axis of the maximum velocity gradient of the bar stars, for a centre at 01h 00m  $-73^{\circ} 00'$ , is shown in green (light grey in the printed version). The other panels show the positions of stars in 50 km s $^{-1}$  bins.

**Table 2.** Weighted mean velocities and  $1\sigma$  standard deviations of the 2dF sample, grouped by spectral classification.

Type	<i>N</i>	$\bar{v}$ [km s $^{-1}$ ]	$\sigma$ [km s $^{-1}$ ]
O	83	$174.1 \pm 0.9$	41.2
B	1251	$175.2 \pm 0.2$	32.1
A	482	$170.9 \pm 0.4$	33.2
FG	229	$160.8 \pm 0.5$	35.1
All	2045	$172.0 \pm 0.2$	33.6
Bar	1572	$167.4 \pm 0.2$	33.3
Wing	473	$189.5 \pm 0.4$	28.6

sample. This region contains the N83 and N84 emission complexes (Henize 1956), and has been noted in the past as having a larger velocity of recession than both the bar and wing populations (e.g. Ardeberg & Maurice 1979; Martin et al. 1989). We also find larger velocities for the 2dF stars in this region:  $\bar{v} = 199.4 \pm 1.7$ ,  $\sigma = 35.6$ , compared to  $\bar{v} = 189.0 \pm 0.4$ ,  $\sigma = 28.1$  for the remaining 446 stars in our wing sample, where we have adopted a radius of  $7.5'$  centred on N84A ( $\alpha = 1\text{h}14\text{m}37\text{s}$ ,  $\delta = -73^{\circ}18'27''$ ; Martin et al. 1989; Bica & Dutra 2000).

### 3.2 Global gradients

To provide a simple quantification of the global velocity gradients in our dataset (Figure 5) we took two approaches. First, as a reasonably nonparametric treatment, we set up a series of spherical-coördinate systems, each defined by a right ascension and declination of zero latitude & longitude (increasing north and east, respectively), with the equatorial great circle rotated by position angle  $\theta$  (measured E from N) from the line of right ascension passing through the central point. For each such system we determined the coefficient of correlation<sup>5</sup> between stellar longitude and radial velocity; where the correlation coefficient  $r$  reaches a maximum, the maximum velocity gradient lies along the equator.

Denoting the position angle of maximum velocity gradient as  $\theta_{\text{max}}$ , we find that the null hypothesis of no velocity gradient can be formally rejected with extremely high confidence ( $> 99.999\%$ ) at  $\theta_{\text{max}}$ , for any chosen central point, with

$$\theta_{\text{max}} \simeq 126^{\circ} + 0.24(50 - \alpha)$$

(where  $\alpha$  is again the right ascension of the adopted central

<sup>5</sup> We computed the Pearson product-moment correlation coefficient  $r$ , Spearman's  $\rho$  statistic, and Kendall's  $\tau$ ; all give sensibly the same results.

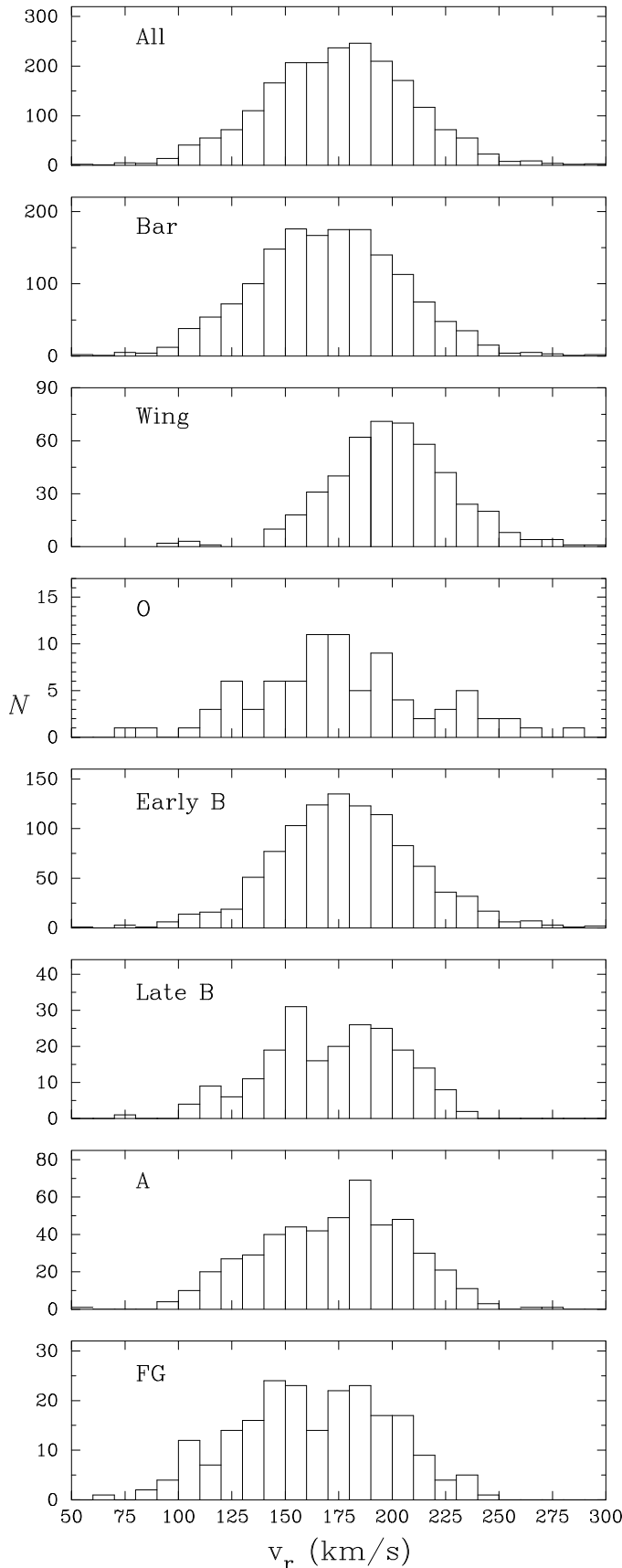


**Figure 6.** Velocity histograms of the 2dF results for the bar and wing sub-samples, and as a function of spectral type.

point in minutes of time, and the optical centre of the SMC is near  $\alpha = 50^m$  – roughly perpendicular to the major axis of optical (and H I) emission. The uncertainty in  $\theta_{\max}$  is of order  $5^\circ$  (see below), while the small variations in  $r(\theta_{\max})$  do not usefully constrain the location of the dynamical centre.

As a more straightforward alternative, we also fit velocities as a simple linear function of position,

$$v = v_0 + A\Delta\alpha + B\Delta\delta,$$

where  $\Delta\alpha$ ,  $\Delta\delta$  are co-ordinate offsets in degrees, measured in cylindrical equidistant projection. This is just a plane, with  $v_0$  the velocity of the plane at the origin of the co-ordinate system. Using the full dataset gives a velocity gradient of  $14.8 \pm 1.0 \text{ km s}^{-1} \text{ deg}^{-1}$  at  $\text{PA} = 127.3 \pm 4.6^\circ$ , with  $v_0 = +173.47 \pm 0.75 \text{ km s}^{-1}$  at  $1^h.0, -73^\circ.0$ .

Figure 7 shows velocities in a co-ordinate system centred on  $01^h 00^m, -73^\circ 00'$  along  $\text{PA} = 126^\circ$ . The velocity gradient here averages  $14.2 \text{ km s}^{-1} \text{ deg}^{-1}$  globally, but evidently most of the velocity change is across the SMC bar. Adopting the previous definition of ‘bar’ and ‘wing’ samples, the 473 stars in the wing show roughly constant velocity (averaging  $+189.5 \text{ km s}^{-1}$ ), while the bar stars show a gradient of  $26.3 \pm 1.6 \text{ km s}^{-1} \text{ deg}^{-1}$  at  $\text{PA} = 126.2 \pm 3.9^\circ$  about a mean velocity of  $167.4 \text{ km s}^{-1}$ . Note that this result is robust to the details of the adopted bar/wing separation, as shown in Table 3.

The amplitude of global velocity changes in our data,  $\sim 50 \text{ km s}^{-1}$ , is comfortably larger than any plausible source of error we have identified. However, although the H I results reported by Staveley-Smith et al. (1997) and Stanimirović et al. (1999) also show more positive velocities in the wing than the bar (i.e., to the SE), the neutral-gas velocity field displays an overall NE/SW dominant gradient. The apparent discrepancy between the NW/SE gradient found here and the SW/NE gradient in the neutral-gas map can be attributed in large part to the region of largest H I velocities lying outside our survey region, around  $1^h 20^m, -71^\circ 30'$  (Fig. 1). This region has a low density of stars (and gas), but purely in terms of H I velocity overwhelms the trend of increasing velocity to the SE which dominates our data, and which is also present in the H I measures.

If we examine our results along the line of maximum gradient identified by Stanimirović et al. (2004, their Fig. 3) we reproduce their results qualitatively, finding a gradient of  $10 \text{ km s}^{-1} \text{ deg}^{-1}$  (along a great circle at  $\text{PA} = 60^\circ$ , through  $\alpha = 0^h 45^m, \delta = -73^\circ$ ; Fig. 7), though this still appears to be somewhat smaller than the neutral-gas gradient.

### 3.3 Induced gradients

An extended source moving perpendicular to the line of sight at its centre is not moving perpendicular to the line of sight elsewhere; the line-of-sight projection of the transverse motion is therefore non-zero other than at the centre. Expressed in terms of observable quantities, the resulting induced velocity gradient is

$$8.273 \times 10^{-2} \frac{\mu}{\text{mas yr}^{-1}} \frac{D}{\text{kpc}} \text{ km s}^{-1} \text{ deg}^{-1}$$

for proper motion  $\mu$  and distance  $D$ .

From observations with the *Hubble Space Telescope* (HST), Kallivayalil et al. (2006) determined a precise proper



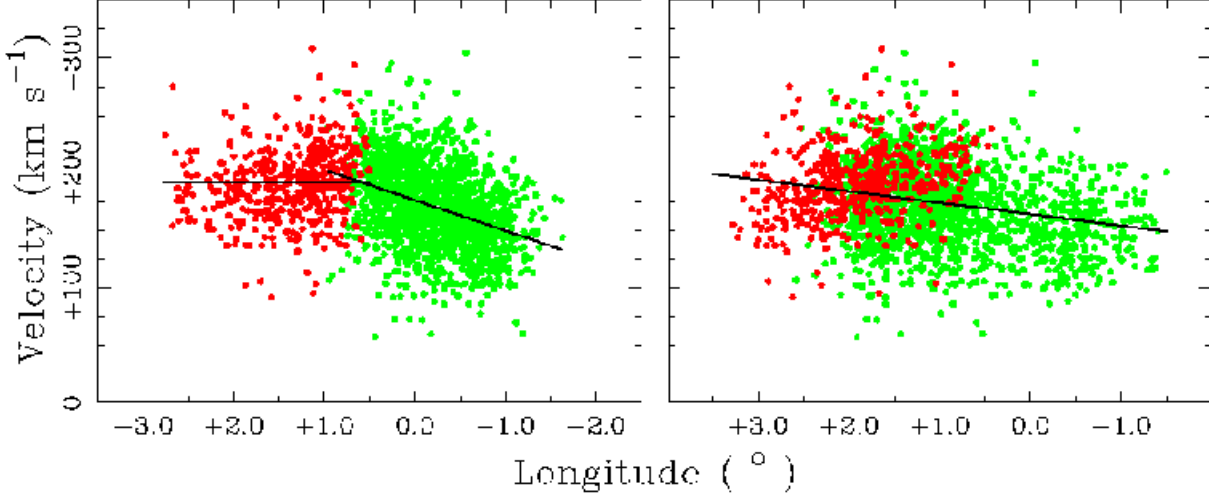


**Figure 7.** *Left:* projection of radial velocities about 01h 00m,  $-73^\circ 0'$  at PA =  $126^\circ$ ; stars assigned to the SMC bar (Section 3) are shown in green (right-hand grouping, light grey in the printed version), with those in the wing shown in red (darker grey). The solid lines show the gradient in the bar ( $26.5 \text{ km s}^{-1} \text{ deg}^{-1}$ ), and the relatively flat gradient further east, in the wing, as discussed in Section 3. *Right:* projection of radial velocities about 0h 45m,  $-73^\circ 0'$  at PA =  $60^\circ$ , the direction of maximum gradient in H I velocities (Section 3); the line has a slope of  $10 \text{ km s}^{-1} \text{ deg}^{-1}$ .

**Table 3.** Velocity gradients derived from 2dF velocities in the SMC bar, as defined by stars north of the lines given in the first column (where  $\alpha$  is the right ascension in minutes of time). Small differences are found depending on the adopted bar/wing separation, but the gradient and position angle are robust.

Southern boundary	N	$\bar{v}$ [ $\text{km s}^{-1}$ ]	Gradient [ $\text{km s}^{-1} \text{ deg}^{-1}$ ]	PA [deg]
$\delta = -77^\circ 50' + (4\alpha)'$	1572	170.8	$26.3 \pm 1.6$	$126.2 \pm 3.9$
$\delta = -77^\circ 20' + (4\alpha)'$	1364	167.7	$24.1 \pm 1.9$	$122.5 \pm 5.3$
$\delta = -78^\circ 20' + (4\alpha)'$	1749	173.4	$25.7 \pm 1.4$	$129.1 \pm 3.3$
$\delta = -79^\circ 50' + (6\alpha)'$	1479	169.6	$27.2 \pm 1.7$	$125.7 \pm 4.0$

motion for the SMC. Such is the interest in their results that Piatek et al. (2008) have recently reanalysed the *HST* data. In Table 4 we list the induced velocity gradients arising from these two measurements, and also for the proper motion results of Kroupa & Bastian (1997) and Irwin (1999). In calculating the induced gradients we adopt  $D = 60.6 \pm 1 \text{ kpc}$  (Hilditch et al. 2005).

The proper motions yield induced velocity gradients in the same general direction as the gradient found in the 2dF results, but their magnitudes are too small to explain our results. Astrophysical and induced gradients will add vectorially, so that the implied magnitude of the residual astrophysical component of the early-type stars is ca.  $18 \text{ km s}^{-1}$ .

Harris & Zaritsky (2006) found a velocity gradient for red giants of  $8.3 \text{ km s}^{-1} \text{ deg}^{-1}$  – about the same magnitude as the induced gradient inferred here from the results of Kallivayalil et al. (2006), but in an almost orthogonal direction (PA =  $23^\circ$ ; that is, roughly along the major axis of the bar). Independent data are required to establish if the absence of induced gradients in red-giant velocities is a result of errors in the measurements (velocities and/or proper motions) or is astrophysical (implying rotation of the red-

giant population about the major axis, in the opposite sense to that found here, to compensate geometrical effects).

### 3.4 Velocity dispersions

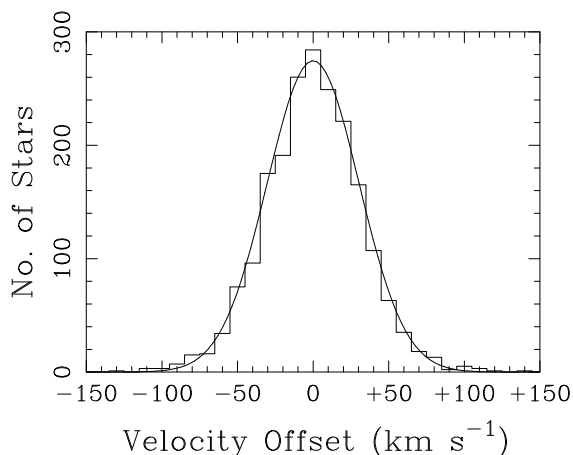
If we take out the large-scale velocity trends in the data by subtracting a simple quadratic fit from the results shown in Fig. 7 (left-hand panel), the weighted  $1\text{-}\sigma$  dispersion of the full set of velocity measurements is reduced from  $33.6 \text{ km s}^{-1}$  to  $30.4 \text{ km s}^{-1}$ . Weighted dispersions for ‘wing’ and ‘bar’ stars are  $28.6$  and  $33.3 \text{ km s}^{-1}$ , respectively; subtracting a linear trend from the bar sample reduces the latter figure to  $30.7 \text{ km s}^{-1}$ , which is not significantly different from the wing value (as judged by an  $F$  test).

Adopting  $30.4 \text{ km s}^{-1}$  as the most representative figure for the observed velocity dispersion, then, assuming that observational and astrophysical contributions sum quadratically, the intrinsic astrophysical velocity dispersion is ca.  $\sim 28 \text{ km s}^{-1}$ . Although Fig. 7 shows that the total velocity range across the observed area of the SMC is substantially larger than this velocity dispersion, most probably that range reflects tidal effects, not rotation. Thus while our observational result contrasts in this respect with Harris &



**Table 4.** Induced velocity gradients from published proper motion results.

Source	$\mu_{\text{west}}$ [mas yr <sup>-1</sup> ]	$\mu_{\text{north}}$ [mas yr <sup>-1</sup> ]	$v_{\text{induced}}$ [ km s <sup>-1</sup> deg <sup>-1</sup> ]	PA [deg]
Kroupa & Bastian (1997)	$-1.23 \pm 0.84$	$-1.21 \pm 0.75$	$8.7 \pm 5.6$	$135 \pm 26$
Irwin (1999)	$-0.92 \pm 0.20$	$-0.69 \pm 0.20$	$5.8 \pm 1.4$	$127 \pm 10$
Kallivayalil et al. (2006)	$-1.16 \pm 0.18$	$-1.17 \pm 0.18$	$8.3 \pm 1.3$	$135 \pm 6$
Piatek et al. (2008)	$-0.75 \pm 0.06$	$-1.25 \pm 0.06$	$7.3 \pm 0.4$	$149 \pm 2$

**Figure 8.** Probability distribution function of radial velocities after correction for systematic gradients (cf. Section 3.4). A gaussian characterized by  $\sigma = 30.4 \text{ km s}^{-1}$  is shown for comparison.

Zaritsky’s result for red giants, we concur that the system is primarily supported by the velocity dispersion.

Interestingly, the velocity dispersion for the O-type spectra (Table 2) is found to be larger than that for the BA stars (at greater than 99% confidence). Weak nebular and/or wind emission could contribute to this, but only one of the 83 O-type stars with measured velocities is commented as having weak emission at  $H\gamma$  (cf. Table A1 from Paper I). It is plausible that undetected emission could be affecting the results, however Balmer emission is as common in the B-type 2dF spectra as in the O-type stars (Table 7 from Paper I), so this does not suggest an explanation for the different dispersions. We also note that the great majority of the O-type stars are either dwarfs or giants, in which wind effects in the higher-order Balmer lines will be relatively minor.

We suggest that the larger dispersion likely originates from undetected massive binaries and runaway stars. The latter suggestion relates to the interesting issue of the relative velocities of field versus cluster stars (aside from the separate issue that 4% of O-type stars appear to form in isolation, de Wit et al. 2005). Using the catalogue of clusters and associations from Bica & Dutra (2000), 18 of our O-type stars with measured velocities are in the field (as defined using the 30 pc criterion from Massey et al. 1995). For the 18 field stars the (weighted) mean is  $\bar{v} = 179.3 \pm 2.2 \text{ km s}^{-1}$  ( $\sigma = 48.9$ ), as compared to  $\bar{v} = 173.2 \pm 0.9 \text{ km s}^{-1}$  ( $\sigma = 39.3$ ) for the 65 others. Unfortunately, with such a limited sample, these results are not statistically significant, but hint at a potentially interesting result, reinforcing the case for a more optimised kinematic survey of the Clouds.

## 4 SUMMARY

We have presented stellar radial velocities measured for 2045 stars from our 2dF survey of the SMC. We find a local velocity dispersion that is approximately gaussian, with  $\sigma \simeq 30$ , similar to recent results for red giants ( $\sigma \simeq 27.5 \text{ km s}^{-1}$ ; Harris & Zaritsky 2006), but the global velocity range is significantly larger, with the SMC wing receding some  $\sim 20 \text{ km s}^{-1}$  faster than the bar. We find a continuous distribution of velocities across the SMC, but those in the wing appear to have a distinct distribution compared to those in the bar (left-hand panel of Fig. 7), presumably a consequence of the last close-interaction between the SMC and LMC  $\sim 0.2 \text{ Gyr}$  ago (Murai & Fujimoto 1980; Yoshizawa & Noguchi 2003; Connors et al. 2006). Within the bar we find a mean gradient of  $26.30 \pm 1.6 \text{ km s}^{-1} \text{ deg}^{-1}$  at  $\text{PA} = 126^\circ$  (cp.  $8.3 \text{ km s}^{-1} \text{ deg}^{-1}$  at  $\text{PA} = 23^\circ$  for the red giants), although, as the H I maps show, this simple parameterization of the data almost certainly disguises a more complex dynamical behaviour.

## 5 ACKNOWLEDGEMENTS

We thank Danny Lennon for the idle conversation on a Friday afternoon at La Cuatro that led to us revisit the 2dF data. We are also grateful to Snezana Stanimirović for her kind permission to use Fig. 1, and the referee for well-informed questions and suggestions. This paper is based on data obtained with the Anglo-Australian Telescope.

## REFERENCES

- Ardeberg A., Maurice E., 1977, A&AS, 30, 261
- Ardeberg A., Maurice E., 1979, A&A, 77, 277
- Besla G., Kallivayalil N., Hernquist L., Robertson B., Cox T. J., van der Marel R. P., Alcock C., 2007, ApJ, 668, 949
- Bica E., Dutra C. M., 2000, AJ, 119, 1214
- Charbonnel C., Meynet G., Maeder A., Schaller G., Schaerer D., 1993, A&AS, 101, 415
- Connors T., Kawata D., Gibson B., 2006, MNRAS, 371, 108
- de Vaucouleurs G., Freeman K. C., 1972, Vistas Astron., 14, 163
- de Wit W. J., Testi L., Palla F., Zinnecker H., 2005, A&A, 437, 247
- Evans C. J., Crowther P. A., Fullerton A. W., Hillier D. J., 2004, ApJ, 610, 1021
- Evans C. J., Howarth I. D., 2003, MNRAS, 345, 1223
- Evans C. J., Howarth I. D., Irwin M. J., Burnley A. W., Harries T. J., 2004, MNRAS, 353, 601, Paper I

- Evans C. J., Lennon D. J., Smartt S. J., Trundle C., 2006, *A&A*, 456, 623
- Gardiner L. T., Noguchi M., 1996, *MNRAS*, 278, 191
- Harries T. J., Hilditch R. W., Howarth I. D., 2003, *MNRAS*, 339, 157
- Harris J., Zaritsky D., 2006, *AJ*, 131, 2514
- Hatzidimitriou D., Cannon R. D., Hawkins M. R. S., 1993, *MNRAS*, 261, 873
- Hatzidimitriou D., Croke B. F., Morgan D. H., Cannon R. D., 1997, *A&AS*, 122, 507
- Henize K. G., 1956, *ApJS*, 2, 315
- Hilditch R. W., Howarth I. D., Harries T. J., 2005, *MNRAS*, 357, 304
- Irwin M., 1999, in Whitelock P., Cannon R., eds, *IAU Symposium 192: The Stellar Content of Local Group Galaxies* ASP, San Francisco, p. 409
- Johnson H. L., 1966, *ARA&A*, 4, 193
- Kallivayalil N., van der Marel R. P., Alcock C., 2006, *ApJ*, 652, 1213
- Kroupa P., Bastian U., 1997, *NewA*, 2, 77
- Kunkel W. E., Demers S., Irwin M. J., 2000, *AJ*, 119, 2789
- Lewis I. J., Cannon R. D., Taylor K., Glazebrook K., Bailey J. A., Baldry I. K., Barton J. R., Bridges T. J., Dalton G. B., Farrell T. J., Gray P. M., Lankshear A., McCowage C., Parry I. R., Sharples R. M., Shortridge K., Smith G. A., Stevenson J., 2002, *MNRAS*, 333, 279
- Martin N., Maurice E., Lequeux J., 1989, *A&A*, 215, 219
- Massey P., 2002, *ApJS*, 141, 81
- Massey P., Lang C. C., DeGioia-Eastwood K., Garmany C., 1995, *ApJ*, 438, 188
- Mathewson D. S., Ford V. L., 1984, in van den Bergh S., de Boer K., eds, *Structure and Evolution of the Magellanic Clouds*, IAU Symposium No. 108 Dordrecht: Reidel, p. 125
- Mathewson D. S., Ford V. L., Visvanathan N., 1988, *ApJ*, 333, 617
- Maurice E., Andersen A., Ardeberg A., Bardin C., Imbert M., Lindgren H., Martin N., Mayor M., Nordström B., Prévot L., Rebeirot E., Rousseau J., 1987, *A&AS*, 67, 423
- McGee R. X., Newton L. M., 1981, *Proc. Astron. Soc. Australia*, 4, 189
- Murai T., Fujimoto M., 1980, *PASJ*, 32, 581
- Piatek S., Pryor C., Olszewski E. W., 2008, *AJ*, in press, arXiv:0712.1764
- Putman M. E., Gibson B. K., Staveley-Smith L., et al. 1998, *Nature*, 394, 752
- Stanimirović S., Staveley-Smith L., Dickey J. M., Sault R. L., Snowden S. L., 1999, *MNRAS*, 302, 417
- Stanimirović S., Staveley-Smith L., Jones P. A., 2004, *ApJ*, 604, 176
- Staveley-Smith L., Sault R. J., Hatzidimitriou D., Kesteven M. J., McConnell D., 1997, *MNRAS*, 289, 225
- Trundle C., Lennon D. J., 2005, *A&A*, 434, 677
- Trundle C., Lennon D. J., Puls J., Dufton P. L., 2004, *A&A*, 417, 217
- Udalski A., Szymański M., Kubiak M., Pietrzyński G., Woźniak P., Żebruń K., 1998, *Acta Astron.*, 48, 147
- Walborn N. R., Lennon D. J., Heap S., Lindler D. J., Smith L. J., Evans C. J., Parker J. W., 2000, *PASP*, 112, 1243
- Yoshizawa A. M., Noguchi M., 2003, *MNRAS*, 339, 1135
- Zaritsky D., Harris J., Thompson I. B., Grebel E. K., Massey P., 2002, *AJ*, 123, 855

## APPENDIX A: CATALOGUE OF STELLAR RADIAL VELOCITIES

The full catalogue of radial velocities for the 2dF sample is available through the on-line edition of *Monthly Notices*, and at the Centre de Données astronomiques de Strasbourg (CDS)<sup>6</sup>.

Table A1 shows an extract from the catalogue, to illustrate the format. For each entry we give coördinates, adopted *B* magnitudes (including their source) and spectral classifications, all from Paper I. In the final three columns we give the mean and standard error (Columns 7 & 8, in  $\text{km s}^{-1}$ ) of the measured velocities, and the number of lines used (Column 9).

<sup>6</sup> <ftp://cdsarc.u-strasbg.fr/pub/cats/J/MNRAS/XXX/YYY>

**Table A1.** An illustrative section of the radial-velocity catalogue. Stellar radial velocities ( $v_r$ ) and the standard error on the mean ( $\sigma/\sqrt{n}$ ) are given in units of  $\text{km s}^{-1}$ ; the final column reports the number of Balmer lines that were measured for each star. Sources of adopted  $B$  magnitudes are Massey (2002), OGLE (Udalski et al. 1998), Zaritsky et al. (2002), and 2dF (i.e. values from the scanned Schmidt plates, see Paper I), coded M, O, Z, and 2 respectively.

2dFS#	$\alpha$ (J2000)	$\delta$ (J2000)	$B$	Source	Spectral type	$v_r$ [ $\text{km s}^{-1}$ ]	$\sigma/\sqrt{n}$ [ $\text{km s}^{-1}$ ]	$n$
0600	00 46 23.13	−72 50 17.4	16.36	O	A3 II	177	19	4
0606	00 46 33.47	−73 39 25.8	13.34	M	B8 (Ib)	203	11	5
0609	00 46 38.10	−73 55 13.7	14.31	Z	B0.5 (IV)	181	38	3
0620	00 46 50.88	−73 55 21.5	14.57	Z	B2 (III)	210	14	5
0625	00 46 55.78	−73 19 56.9	14.32	Z	B9 (Ib)	130	7	5
0628	00 46 57.87	−73 15 40.0	20.24	O	B1-5 (V)	151	8	4
0629	00 47 01.39	−74 08 33.6	15.21	Z	A2 II	186	14	4
0630	00 47 01.70	−72 35 05.2	15.03	Z	A0 (Ib)	180	4	5
0636	00 47 12.95	−73 53 33.1	14.71	Z	B2 (III)	119	7	5
0637	00 47 14.46	−73 25 39.6	15.40	Z	B0-5 (III)	145	20	4
0644	00 47 23.47	−73 33 35.0	14.58	O	B0-5 (II)	165	26	3
0646	00 47 24.04	−72 37 37.3	14.46	Z	A5 II	155	13	4
0648	00 47 26.78	−73 32 03.4	16.53	Z	A3 II	199	16	3